RETRACTED: Realization of chiral multifold semimetal RhSi crystalline thin films

Hua Lv,[1,*,†] Edouard Lesne,[1,*,‡] Rebeca Ibarra,[1] Yan Sun,[2] Anastasios Markou,[1,3,§] and Claudia Felser[1,**]

[1]*Max Planck Institute for Chemical Physics of Solids, Nöthnitzer Str. 40, 01187 Dresden, Germany*

[2]*Institute of Metal Research, Chinese Academy of Science, Shenyang, China*

[3]*Physics Department, University of Ioannina, 45110 Ioannina, Greece*

(Received 4 January 2023; accepted 5 May 2023; published 26 May 2023)

Nonmagnetic topological semimetals that combine chirality in real and momentum spaces host unconventional multifold fermions and exhibit exotic electronic and optical properties endowed by their topologically nontrivial electronic band structure. Although the synthesis of nonmagnetic chiral single crystals with a noncentrosymmetric cubic B20 structure is well established, their heteroepitaxial growth in crystalline thin films remains a notable challenge. In this study, we present the structural, magnetic, and electrical magnetotransport properties of 24- and 51-nm-thick films of a B20-RhSi stoichiometric compound grown by magnetron sputtering. RhSi crystalline thin films on Si (111) single-crystal substrates exhibit a preferred (111) orientation with twin domains. The RhSi films display a nonmagnetic ground state, and their electrical resistivity demonstrates a clear and nonsaturating metallic behavior from 300 to 5 K. Magnetotransport measurements reveal that hole-type carriers dominate the Hall response with multiband contributions to electronic transport in the system. The good agreement with the Bloch-Grüneisen model and our first-principles calculations confirms that temperature-dependent electrical resistivity is governed by electron-phonon scattering. The ability to grow textured-epitaxial thin films of nonmagnetic B20 chiral topological semimetals is an important step toward accessing and controlling their remarkable topological surface states for designing chiraltronic devices with novel optoelectronic or spintronic functionalities.

DOI: 10.1103/PhysRevMaterials.7.054201

I. INTRODUCTION

Over the past few years, chiral crystals have opened a new research direction in condensed-matter physics because of their symmetry-related exotic physical properties [1]. Among the chiral crystals, topological chiral semimetals with a noncentrosymmetric cubic FeSi-type structure (B20-type structure) and space group $P2_13$ (No. 198) are of particular interest because they display chirality in their crystal, magnetic, and electronic structures [2–5]. The crystal structure of these materials is characterized by two enantiomers with right- and left-handed atomic arrangements of opposite chirality; these enantiomers with right (*R*)- and left (*L*)-handedness are categorized into two inequivalent notations: *RL* and *LR*. The *RL* notation indicates that the sublattice of the transition metal atom (rhodium) has an *R*-type structure, the sublattice of the metalloid atom (silicon) has an *L*-type structure, and vice versa for the *LR* notation, as indicated in Figs. 1(a)–1(d). The atomic arrangements of enantiomers break inversion and mirror symmetries while conserving the rotational symmetries. The broken-inversion symmetry and strong spin-orbit coupling in magnetic B20 compounds yield a Dzyaloshinskii-Moriya exchange interaction [6,7], which results in chiral magnetic topological excitations [3,8]. In addition to magnetic compounds, the B20 family includes nonmagnetic compounds such as RhSi, CoSi, PdGa, and PtAl. These crystals host multifold fermions in their electronic structure because of topological band crossings where more than two bands meet with higher Chern numbers and larger Fermi arcs than those of Weyl and Dirac semimetals [2,9–15]. The multifold fermions of these compounds cause several remarkable effects forbidden in other topological classes, such as quantized circular photogalvanic effects [16–19] and gyrotropic and chiral magnetic effects [20,21].

In this study, we focus on the nonmagnetic chiral topological semimetal RhSi, which crystallizes in the aforementioned B20-type structure, with bulk lattice constants of $a = b = c = 4.674$ Å [Figs. 1(a)–1(d)]. Rh and Si atoms occupy the Wyckoff position 4*a*. Photoemission spectroscopy experiments have revealed giant topological Fermi arcs with a helicoid structure and Chern number of ± 2 [11,22]. Additionally, linear and nonlinear optical responses have been confirmed in single crystals of RhSi, derived from the chirality of the electronic structure and multifold fermions [23–27].

*These authors contributed equally to this work.

†Present address: Paul-Drude-Institut für Festkörperelektronik, Leibniz-Institut im Forschungsverbund Berlin e.V., Hausvogteiplatz 5-7, 10117 Berlin, Germany.

‡Corresponding author: Edouard.Lesne@cpfs.mpg.de

§Corresponding author: Anastasios.Markou@cpfs.mpg.de

**Corresponding author: Claudia.Felser@cpfs.mpg.de

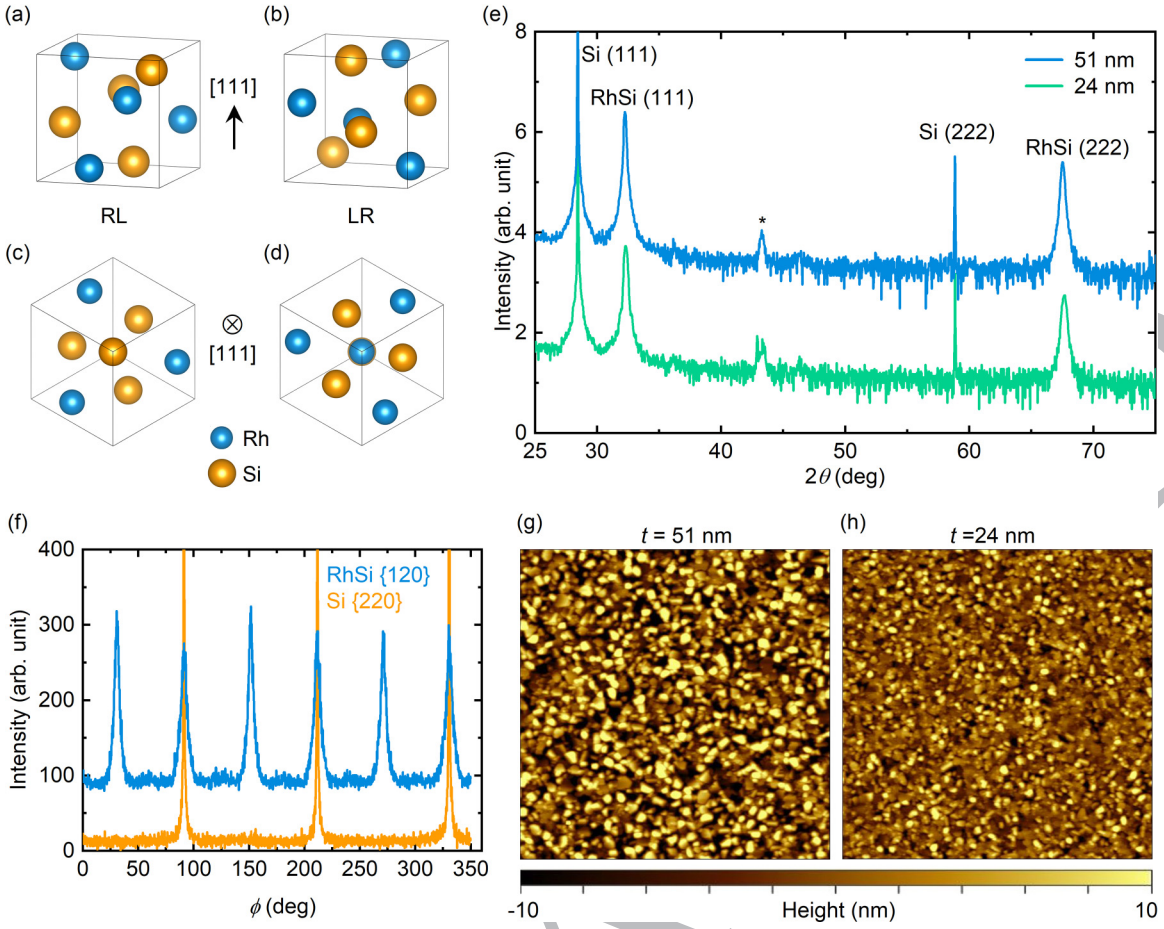

FIG. 1. Structural properties of (111)-oriented RhSi crystalline thin films. (a), (b) Illustration of the B20-RhSi enantiomorphous pair of crystal structures with opposite chirality. The *RL* notation indicates that the Rh is an *R*-type structure, whereas Si is an *L*-type structure; the opposite occurs for the *LR* notation. Blue and orange spheres depict the Rh and Si atoms, respectively. (c), (d) Both enantiomorphous pair of structures are shown along the [111] crystallographic direction. (e) 2θ-ω XRD pattern of the RhSi (111) films of different thicknesses. The asterisk denotes the (120) Bragg reflection. (f) Azimuthal φ scans of the {120} family of planes of the 51-nm-thick RhSi film and {220} planes of the Si substrate. (g), (h) Topographic AFM images of the RhSi films with different thicknesses and without a capping layer. AFM images are 5 μm × 5 μm.

In addition to its exotic optical properties, RhSi exhibits enantioselectivity in heterogeneous catalytic processes [28]. Although most studies focused on single crystals of nonmagnetic chiral topological semimetals, textured-epitaxial thin films of silicide B20 compounds are yet to be explored.

In this paper, we present the crystalline growth of 24- and 51-nm-thick RhSi films on Si (111) substrates by magnetron sputtering. Our textured-epitaxial films possess distinct crystallographic features and electronic responses with respect to bulk crystals. The out-of-plane lattice parameters are larger by more than 2%, and the in-plane lattice parameters are comparable with the bulk crystals, as revealed by x-ray-diffraction (XRD) measurements. In addition, the RhSi films exhibit a hole-type ordinary Hall effect with nonlinearities in the magnetic field indicative of multiband conduction.

II. EXPERIMENTAL DETAILS

Using a BESTEC ultrahigh-vacuum magnetron sputtering system, 24- and 51-nm-thick (111)-textured RhSi films were grown on (111)-oriented Si single-crystal substrates. Before the thin-film growth, we chemically treated the Si substrates to remove the native oxide using 2% hydrofluoric acid for 3 min, followed by *in situ* annealing at 850° C for 20 min in the sputtering chamber. Before deposition, the chamber was evacuated to a base pressure of less than 8×10^{-9} mbar, whereas the process gas (Ar 5 N) pressure was 3×10^{-3} mbar. The target-to-substrate distance was 20 cm, and the substrates were rotated at 24 rpm to ensure homogeneous growth. We used Rh (5.08 cm) and Si (7.62 cm) sources in confocal geometry by applying 15-W dc power and 80-W rf power for the deposition of stoichiometric RhSi thin films, respectively. The films were grown at 680° C and capped with an amorphous 3-nm-thick Si film deposited at room temperature to prevent the oxidation of the film.

Stoichiometry was estimated as $Rh_{49}Si_{51}$ by energy-dispersive x-ray spectroscopy with an experimental uncertainty of 3%. Symmetric and asymmetric XRD, as well as x-ray reflectivity (XRR) scans were conducted with a Panalytical X'Pert^3 MRD diffractometer using Cu $K\alpha_1$ radiation ($\lambda = 1.5406$ Å). The growth rate and film thickness were determined by XRR measurements. Surface morphology

was measured using atomic force microscopy (AFM) with an Asylum Research MFP-3D Origin (Oxford Instruments). Magnetization measurements were performed using a Quantum Design magnetometer [MPMS3 superconducting quantum interference device (SQUID)-VSM]. Electrical (magneto-)transport measurements were carried out in a PPMS9 Quantum Design cryostat in van der Pauw geometry using ultrasonically bonded Al wires to contact the corners of the square sample. We sourced a 100-μA low-frequency (128.23-Hz) alternating current (I) and used a standard lock-in amplifier detection technique to measure either the longitudinal (V_{xx}) or transverse (V_{xy}) voltages. Consequently, the longitudinal and Hall resistivities are given by $\rho_{xx} = (V_{xx}/I)[\pi/\ln(2)]t$ and $\rho_{xy} = (V_{xy}/I)t$, respectively, with t being the film thickness determined by the XRR.

The electronic band structure of RhSi was calculated using the Vienna *Ab initio* Simulation Package (VASP) [29] considering the experimentally measured lattice constants and theoretically relaxed atomic positions. The exchange and correlation energies were conserved in the generalized gradient approximation [30].

III. RESULTS AND DISCUSSION

Figure 1 shows the structural characterization and topographic imaging of the textured-epitaxial RhSi films. Figure 1(e) shows the symmetric 2θ-ω XRD radial scan of the 24- and 51-nm-thick RhSi films grown on Si (111) single-crystalline substrates. In both films, the predominantly (111) family of (hkl) Bragg reflections of cubic RhSi is indicative of (111)-oriented films. A low-intensity reflection appeared at 43.27°, which corresponds to the (120) reflection, with less than 1% of the total integrated reflection intensity. Moreover, we performed asymmetric azimuthal XRD scans to probe the in-plane epitaxial relationship between the RhSi film and Si substrate. Figure 1(f) depicts the XRD azimuthal scans of the Si {220} and RhSi {120} families of planes for the 51-nm-thick film. The cubic Si single-crystal substrate shows three peaks at 120° ($2\pi/3$) intervals, which reflects the threefold rotational symmetry of the crystal. Figures 1(c)–1(d) show that a threefold rotational symmetry along the [111] axis is expected for a RhSi single crystal; however, the RhSi film exhibits six reflections with $2\pi/6$ periodicity, which indicates a sixfold symmetry. The occurrence of sixfold symmetry in the RhSi film with an almost equal intensity of reflections at 60° intervals can be attributed to the existence of twin domains, which is similar to the B20-MnSi films grown by molecular-beam epitaxy [31]. Thus, at present, RhSi films are stabilized with a (111) textured-epitaxial orientation, with both left- and right-handed chiral grains (or enantiomers) with an overall equal volume distribution within the film [Figs. 1(c) and 1(d)].

The lattice parameter of the bulk RhSi compound is 14% smaller than that of Si. Therefore, RhSi films can favorably grow on Si(111) substrates with an azimuthal rotation of 30°, which reduces the mismatch between film and substrate to a mere 0.6%. Therefore, from the symmetric and asymmetric XRD scans, we conclude that the epitaxial relationship between the (111)-oriented film and substrate is

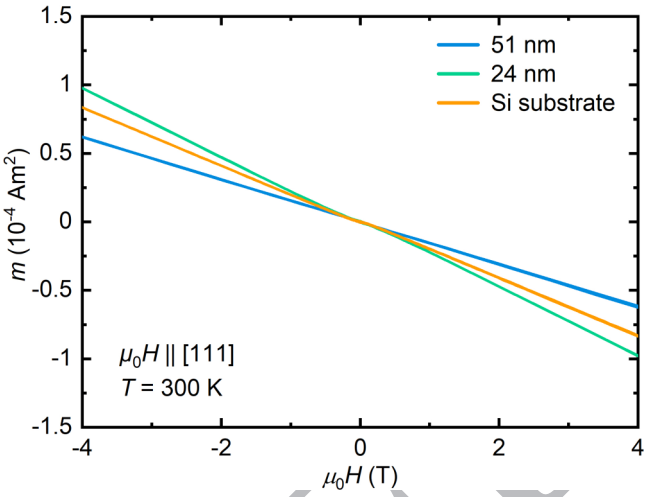

FIG. 2. Curves of the magnetic moment as a function of the external magnetic field for the 51- and 24-nm-thick RhSi films. μ_0H is applied along the [111] crystal axis of RhSi, at 300 K. For comparison, we include the magnetization curve of a Si(111) substrate measured under the same conditions (μ_0H out of plane).

RhSi(111)[$\bar{1}10$] ∥ Si(111)[$\bar{1}\bar{1}2$]. In addition, we calculated the out-of-plane (c-lattice parameter) and in-plane (a-lattice parameter) lattice parameters from the positions of the symmetric (111) and asymmetric (120) families of Bragg peaks, respectively. The 51-nm-thick film has lattice parameters of $c = 4.803$ Å and $a = b = 4.674$ Å, and the 24-nm-thick film has $c = 4.796$ Å and $a = b = 4.663$ Å, which indicate a strain-induced rhombohedral distortion in RhSi films caused by the lattice mismatch between the film and the substrate.

Finally, we mapped the surface topographies of the RhSi films. We grew replicas of nominally identical thicknesses of the RhSi films investigated in this study, but without a capping layer for AFM imaging. Figures 1(g) and 1(h) show topographic images of RhSi films with thicknesses of 51 and 24 nm, respectively. Both films were uniform, continuous, and showed no signs of dislocations. The surfaces of the 51- and 24-nm-thick RhSi films are relatively rough and characterized by a root-mean-square roughness of 6.2 and 3.8 nm, respectively.

Figure 2 shows the curves of the magnetic moment as a function of the magnetic field (μ_0H) of the 51- and 24-nm-thick RhSi films and the Si substrate, which we collected with the μ_0H applied parallel to the [111] axis of RhSi at 300 K. The RhSi films (on Si substrates) show a diamagnetic signal with no net moment (m) at zero field, and with a slope and magnitude uncorrelated to the RhSi thickness and similar to those measured on a reference Si single-crystalline substrate. We find a qualitatively similar behavior at 50 K (not shown) for both films and Si reference substrate, and conclude that the RhSi films do not exhibit a magnetically ordered state.

Figure 3 shows the band structures of the RhSi films. The energy dispersion along high-symmetry lines shows that the film and bulk forms of RhSi share similar band structures [11,24]. However, the experimental lattice parameters of the films are rhombohedrally distorted, which cause the cubic symmetry to be broken; considering this leads to the

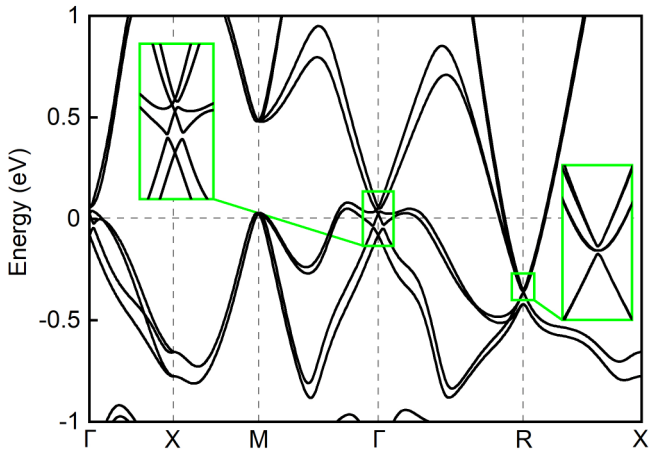

FIG. 3. Electronic band structure of the RhSi (111) compound which includes spin-orbit coupling, and using the experimentally determined lattice parameters of the thicker film. Insets at the Γ and *R* points highlight specific energy ranges that host highly degenerate Fermionic bands. The Fermi energy is taken as $E_F = 0$, and it is represented by the horizontal dashed line.

splitting of the sixfold and fourfold degeneracies at the *R* and Γ points, respectively. Spin degeneracy is protected only by time-reversal symmetry at these two points, as indicated in the zoomed-in electronic structure around the *R* and Γ points. Therefore, the energy degeneracy of the three doubly degenerated points at point *R* is lifted by only ∼ 3 meV. In comparison, energy splitting at the Γ point for the generated double degeneracy is ∼ 30 meV, which is considerably larger than the state-of-the art resolution of band-structure measurement techniques such as angle-resolved photoelectron spectroscopy (ARPES) and scanning tunneling microscopy. Therefore, the changes in the original fourfold fermions at the Γ point are experimentally measurable.

Now, we turn to the electrical and magnetotransport measurements performed in a van der Pauw configuration, as detailed in Sec. II. Figure 4(a) shows the temperature dependence of the longitudinal resistivity ρ_{xx} (T) of the (111)-oriented RhSi films. ρ_{xx} (T) shows a metallic behavior with a continuous decrease on cooling the 24- and 51-nm RhSi films from 300 to 5 K. The thinner film displays a lower resistivity than the thicker one across the entire temperature range, with a residual resistivity as low as 112.5 μΩ cm at 5 K. In addition, the resistivity does not show saturation. This indicates that in the spirit of Matthiessen's rule, and excluding magnetic ordering in our RhSi films, in the investigated temperature range: $\rho_{xx}(T)$ is not governed by extrinsic scattering mechanisms at, e.g., grain boundaries, impurities, interfaces, or crystallographic defects (whose prominence would yield a higher residual resistivity in the thinnest film). At this stage, we can only hypothesize the role played by epitaxial strain and distortion on the electronic transport of RhSi films, which should stimulate further investigation.

We further assessed the electron scattering mechanism that governs the *T*-dependent resistivity using the Bloch-Grüneisen (BG) model [32–34] given as

$$\rho_{xx}(T) = \rho_0 + A\left(\frac{T}{\Theta_{BG}}\right)^n \int_0^{\frac{\Theta_{BG}}{t}} \frac{t^n}{(e^t - 1)(1 - e^t)} dt, \quad (1)$$

where Θ_{BG} represents the Bloch-Grüneisen temperature, ρ_0 is considered in the model as $\rho_{xx}(T = 10\,\mathrm{K})$, and $n = 5$ for electron-phonon scattering, characteristically; therefore, *A* parametrizes the electron-phonon scattering strength. The temperature dependence of the measured ρ_{xx} (T) curves is described by Eq. (1) [dashed black lines in Fig. 4(a)] with $n = 5$. The BG model yields an effective BG temperature $\Theta_{BG} = 143$ and 163 K for the 24- and 51-nm films, respectively. Θ_{BG} is approximately three times smaller than the calculated Debye temperature for the bulk RhSi crystals [35]; this suggests that the scattering of carriers with the Fermi wave vector considerably smaller than π/a (first Brillouin-zone boundary) caused by acoustic phonons is progressively suppressed when the temperature is reduced below 300 K. Indeed, the Fermi surface of the metallic RhSi demonstrated via the combination of ARPES measurements and first-principle calculations [11,22] hosts both electron and hole pockets (at the Γ and *M* points connected by Fermi arcs); their characteristic Fermi

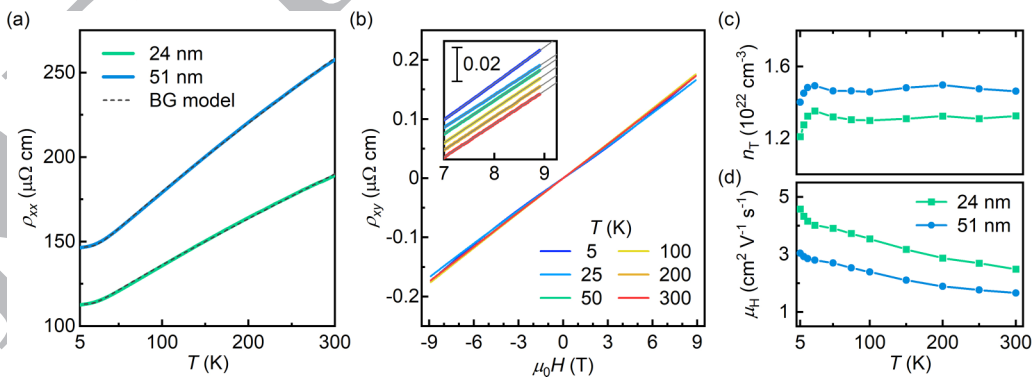

FIG. 4. Electrical transport properties of RhSi crystalline thin films. (a) Longitudinal resistivity vs temperature [$\rho_{xx}(T)$] shows good agreement for each film (24 and 51 nm) between the experimental data and the BG model following Eq. (1). (b) Ordinary Hall resistivity (ρ_{xy}) under an external out-of-plane magnetic field at various temperatures, for the 24-nm-thick RhSi film. $\rho_{xy}(H)$ traces evidence a Hall effect dominated by holelike carriers, and exhibit nonlinearities characteristic of multiband conduction. Inset: linear fits to the Hall traces above 7 T. Traces have been vertically offset for clarity. (c) Temperature dependence of the total carrier density (n_T) and (d) carrier mobility (μ_H) for the two films' thicknesses.

wave vector is very sensitive to E_F and evolves dramatically with respect to shifts in the Fermi energy by only a few meV. Our calculations fully concur with these observations using experimentally measured lattice parameters, and with the strongly dispersive nature of the bands at both the Γ and M points (insets of Fig. 3).

Figure 4(b) shows the field-antisymmetrized Hall resistivity as a function of the applied magnetic field along the [111] out-of-plane direction for the 24-nm-thick RhSi film. We observed an ordinary Hall effect with an overall positive slope throughout the entire measured temperature range; this is indicative of the electronic transport dominated by the hole-type carriers. Further, we observe that at temperatures higher than 250 K and lower than 50 K the Hall traces show a pronounced nonlinear behavior commonly attributed to multiband transport (of either multiple holelike, or hole- and electron-like carriers) [36]. In contrast, the Hall effect displays little nonlinearity in the intermediate temperature range ($50\,\mathrm{K} < T < 250\,\mathrm{K}$). Overall, these observations provide a natural explanation following the discussions carried out regarding the complex Fermi surface of RhSi with its expected multiple electron and holelike pockets whose sizes are susceptible to slight changes ($< 10\,\mathrm{meV}$) in the Fermi energy. The applicability of a two-band scenario to fit the Hall traces, although desirable, cannot unequivocally assess the absolute carrier densities (n_1, n_2) and mobilities (μ_1, μ_2) of each band (indexed as 1 and 2) because of a lack of constraints on the model's fitting parameters. The concomitant measurement of the magnetoresistance and Hall effect in a Hall bar geometry, as well as resorting to larger magnitudes of the external magnetic field, can help constrain the model and unravel the nature of the various contributing holelike or hole- and electron-like bands.

However, we can estimate the total carrier densities $n_T = (n_1 + n_2)$ independently of the type of the carriers in either band, which in a two-band model can be deduced from the "high-field" slope of the Hall effect provided the response is purely linear in the field. The total charge-carrier density is then given by $n_T = 1/(R_H \cdot q)$, with $q = e$, the elementary charge, and R_H the high-field Hall coefficient, i.e., the slope of $\rho_{xy}(H > 7\,\mathrm{T})$; see inset of Fig. 4(b). The results are displayed as a function of the temperature in Fig. 4(c). Remarkably, the total carrier density was found to be nearly temperature independent for both films and reached values of approximately 1.3 and $1.5 \times 10^{22}\,\mathrm{cm}^{-3}$ for the 24- and 51-nm films, respectively. Figure 4(d) shows the temperature dependence of the field-independent average carrier mobility from the Hall measurements estimated according to $\mu_H = 1/(\rho_{xx} \cdot n_T \cdot e)$. The carrier mobility was found to continuously increase upon decreasing the temperature [see Fig. 4(d)] with no sign of saturation at low temperature; this is noteworthy for metallic thin films and indicates that the electronic conductivity of the crystalline RhSi textured films reported here is not limited, down to 5 K, by scattering arising from disorder, crystallographic defects, or impurities. The electronic mobility is found to be larger than $4\,\mathrm{cm}^2\mathrm{V}^{-1}\,\mathrm{s}^{-1}$ for the 24-nm film below 5 K, which remains orders of magnitude lower than in some other bulk B20 single crystals [14,37,38], but of the same order of magnitude as that of other thin films of trivial and topological metals [39–42].

IV. CONCLUSION

We grew 24- and 51-nm-thick textured-epitaxial films of chiral multifold semimetal RhSi on Si (111) substrates. The RhSi films have a strong preferential (111) orientation, and the sixfold symmetry of azimuthal φ scans of asymmetric reflection signals twin domains, which is indicative of an approximately equal fraction of right- and left-handed enantiomorphous crystalline grains. SQUID magnetometry measurements confirmed that the RhSi films were nonmagnetic, and the electrical transport measurements revealed metallic behavior down to the lowest temperatures with a low residual resistivity not dominated by defects or impurity scattering down to 5 K. We find good agreement between the $\rho_{xx}(T)$ experimental data and the BG model, which establishes electron-phonon scattering as the leading cause of the decrease in electrical conductivity with an increasing temperature. Finally, RhSi films exhibit an ordinary Hall effect of hole-type carriers with nearly temperature-independent electronic densities and electronic mobilities that continuously increase upon lowering the temperature, reaching $4.5\,\mathrm{cm}^2\mathrm{V}^1\mathrm{s}^{-1}$ below 10 K. The work presented here represents an important step towards the realization of functional devices made of nonmagnetic multifold fermion B20 compounds compatible with silicon-based electronics.

The study of crystalline thin films of chiral B20 topological metals is expected to provide fundamental insights into their intertwined electronic, chemical, and physical properties. In addition to composition/doping control, heteroepitaxial thin films offer film thickness and strain as tuning parameters, which cannot be explored in bulk crystals. Moreover, heterostructures of nonmagnetic B20 compounds with other quantum materials, e.g., superconductors (SC), (anti)ferromagnets, or topological semimetals, are expected to open up the study of superconducting proximity effects (such as Josephson diode effects in noncentrosymmetric SC [43]), spin- and orbital Hall effects [39], current-induced spin selectivity [44,45], and electrical magnetochiral anisotropy [46], while enabling the integration of these chiral materials into functional spintronic and electro-optical devices [47].

ACKNOWLEDGMENTS

We thank S. Galeski, H. Lin, and L. Zhang for discussions. This work was supported by the Horizon 2020 FETPROAC Project No. SKYTOP-824123—"Skyrmion—Topological Insulator and Weyl Semimetal Technology" and the Sächsische Aufbaubank - Förderbank - (SAB) project Topologische Spintronic: CMOS-kompatible Materialien aus der B20-Familie (TOP20), Clusternr. No. 4188.

[1] G. Q. Chang, B. J. Wieder, F. Schindler, D. S. Sanchez, I. Belopolski, S. M. Huang, B. Singh, D. Wu, T. R. Chang, T. Neupert, S. Y. Xu, H. Lin, and M. Z. Hasan, Nat. Mater. **17**, 978 (2018).

[2] B. Bradlyn, J. Cano, Z. Wang, M. G. Vergniory, C. Felser, R. J. Cava, and B. A. Bernevig, Science **353**, aaf5037 (2016).

[3] S. Mühlbauer, B. Binz, F. Jonietz, C. Pfleiderer, A. Rosch, A. Neubauer, R. Georgii, and P. Böni, Science **323**, 915 (2009).

[4] G. H. Fecher, J. Kübler, and C. Felser, Materials **15**, 5812 (2022).

[5] P. Narang, C. A. C. Garcia, and C. Felser, Nat. Mater. **20**, 293 (2021).

[6] I. Dzyaloshinsky, J. Phys. Chem. Solids **4**, 241 (1958).

[7] T. Moriya, Phys. Rev. **120**, 91 (1960).

[8] X. Z. Yu, N. Kanazawa, Y. Onose, K. Kimoto, W. Z. Zhang, S. Ishiwata, Y. Matsui, and Y. Tokura, Nat. Mater. **10**, 106 (2011).

[9] P. Tang, Q. Zhou, and S.-C. Zhang, Phys. Rev. Lett. **119**, 206402 (2017).

[10] D. Takane, Z. Wang, S. Souma, K. Nakayama, T. Nakamura, H. Oinuma, Y. Nakata, H. Iwasawa, C. Cacho, T. Kim, and K. Horiba, H. Kumigashira, T. Takahashi, Y. Ando, and T. Sato, Phys. Rev. Lett. **122**, 076402 (2019).

[11] D. S. Sanchez, I. Belopolski, T. A. Cochran, X. Xu, J.-X. Yin, G. Chang, W. Xie, K. Manna, V. Süß, C.-Y. Huang, N. Alidoust, D. Multer, S. S. Zhang, N. Shumiya, X. Wang, G.-Q. Wang, T.-R. Chang, C. Felser, S.-Y. Xu, S. Jia, H. Lin, and M. Z. Hasan, Nature (London) **567**, 500 (2019).

[12] Z. Rao, H. Li, T. Zhang, S. Tian, C. Li, B. Fu, C. Tang, L. Wang, Z. Li, W. Fan, J. Li, Y. Huang, Z. Liu, Y. Long, C. Fang, H. Weng, Y. Shi, H. Lei, Y. Sun, T. Qian, and H. Ding, Nature (London) **567**, 496 (2019).

[13] N. B. M. Schröter, S. Stolz, K. Manna, F. de Juan, M. G. Vergniory, J. A. Krieger, D. Pei, T. Schmitt, P. Dudin, T. K. Kim, C. Cacho, B. Bradlyn, H. Borrmann, M. Schmidt, R. Widmer, V. N. Strocov, and C. Felser, Science **369**, 179 (2020).

[14] M. Yao, K. Manna, Q. Yang, A. Fedorov, V. Voroshnin, B. V. Schwarze, J. Hornung, S. Chattopadhyay, Z. Sun, S. N. Guin, J. Wosnitza, H. Borrmann, C. Shekhar, N. Kumar, J. Fink, Y. Sun, and C. Felser, Nat. Commun. **11**, 2033 (2020).

[15] M. Z. Hasan, G. Chang, I. Belopolski, G. Bian, S. -Y. Xu, and J. -X. Yin, Nat. Rev. Mater. **6**, 784 (2021).

[16] F. de Juan, A. G. Grushin, T. Morimoto, and J. E. Moore, Nat. Commun. **8**, 15995 (2017).

[17] F. Flicker, F. de Juan, B. Bradlyn, T. Morimoto, M. G. Vergniory, and A. G. Grushin, Phys. Rev. B **98**, 155145 (2018).

[18] G. Chang, J.-X. Yin, T. Neupert, D. S. Sanchez, I. Belopolski, S. S. Zhang, T. A. Cochran, Z. Cheng, M.-C. Hsu, S.-M. Huang, B. Lian, S.-Y. Xu, H. Lin, and M. Z. Hasan, Phys. Rev. Lett. **124**, 166404 (2020).

[19] C. Le, Y. Zhang, C. Felser, and Y. Sun, Phys. Rev. B **102**, 121111(R) (2020).

[20] S. Zhong, J. E. Moore, and I. Souza, Phys. Rev. Lett. **116**, 077201 (2016).

[21] J. Ma and D. A. Pesin, Phys. Rev. B **92**, 235205 (2015).

[22] G. Chang, S.-Y. Xu, B. J. Wieder, D. S. Sanchez, S.-M. Huang, I. Belopolski, T.-R. Chang, S. Zhang, A. Bansil, H. Lin, and M. Z. Hasan, Phys. Rev. Lett. **119**, 206401 (2017).

[23] D. Rees, K. Manna, B. Lu, T. Morimoto, H. Borrmann, C. Felser, J. E. Moore, D. H. Torchinsky, and J. Orenstein, Sci. Adv. **6**, eaba0509 (2020).

[24] Z. Ni, B. Xu, M. A. Sánchez-Martínez, Y. Zhang, K. Manna, C. Bernhard, J. W. F. Venderbos, F. de Juan, C. Felser, A. G. Grushin, and L. Wu, npj Quantum Mater. **5**, 96 (2020).

[25] L. Z. Maulana, K. Manna, E. Uykur, C. Felser, M. Dressel, and A. V. Pronin, Phys. Rev. Res. **2**, 023018 (2020).

[26] D. Rees, B. Lu, Y. Sun, K. Manna, R. Özgür, S. Subedi, H. Borrmann, C. Felser, J. Orenstein, and D. H. Torchinsky, Phys. Rev. Lett. **127**, 157405 (2021).

[27] B. Lu, S. Sayyad, M.-Á. Sánchez-Martínez, K. Manna, C. Felser, A. G. Grushin, and D. H. Torchinsky, Phys. Rev. Res. **4**, L022022 (2022).

[28] G. Li, Q. Yang, K. Manna, Y. Zhang, P. Merz, C. Shekhar, H. Lv, A. Markou, Y. Sun, and C. Felser, Angew. Chem. e202303296 (2023).

[29] G. Kresse and J. Hafner, Phys. Rev. B **48**, 13115 (1993).

[30] J. P. Perdew, K. Burke, and M. Ernzerhof, Phys. Rev. Lett. **77**, 3865 (1996).

[31] M. Trabel, N. V. Tarakina, C. Pohl, J. A. Constantino, C. Gould, K. Brunner, and L. W. Molenkamp, J. Appl. Phys. **121**, 245310 (2017).

[32] F. Bloch, Z. Phys. **59**, 208 (1930).

[33] E. Grüneisen, Ann. Phys. Leipzig **408**, 530 (1933).

[34] H. L. Stormer, L. N. Pfeiffer, K. W. Baldwin, and K. W. West, Phys. Rev. B **41**, 1278 (1990).

[35] J.-J. Wang, A. Hermann, X.-Y. Kuang, Y.-Y. Jin, C. Lu, C.-Z. Zhang, M. Ju, M.-T. Si, and T. Iitaka, RSC Adv. **5**, 53497 (2015).

[36] N. W. Ashcroft and N. D. Mermin, *Solid State Physics* (Harcourt Brace College Publishers, New York, 1976).

[37] S. Sasmal, G. Dwari, B. B. Maity, V. Saini, A. Thamizhavel, and R. Mondal, J. Phys.: Condens. Matter **34**, 425702 (2022).

[38] V. Saini, S. Sasmal, R. Kulkarni, B. Singh, A. Thamizhavel, A. Nakamura, and D. Aoki, Phys. Rev. B **106**, 125126 (2022).

[39] K. Tang, Y.-C. Lau, K. Nawa, Z. Wen, Q. Xiang, H. Sukegawa, T. Seki, Y. Miura, K. Takanashi, and S. Mitani, Phys. Rev. Res. **3**, 033101 (2021).

[40] J. M. Taylor, A. Markou, E. Lesne, P. K. Sivakumar, C. Luo, F. Radu, P. Werner, C. Felser, and S. S. P. Parkin, Phys. Rev. B. **101**, 094404 (2020).

[41] A. Markou, D. Kriegner, J. Gayles, L. Zhang, Y.-C. Chen, B. Ernst, Y.-H. Lai, W. Schnelle, Y.-H. Chu, Y. Sun, and C. Felser, Phys. Rev. B **100**, 054422 (2019).

[42] A. Markou, J. Gayles, E. Derunova, P. Swekis, J. Noky, L. Zhang, M. N. Ali, Y. Sun, and C. Felser, Commun. Phys. **4**, 104 (2021).

[43] F. Ando, Y. Miyasaka, T. Li, J. Ishizuka, T. Arakawa, Y. Shiota, T. Moriyama, Y. Yanase, and T. Ono, Nature (London) **584**, 373 (2020).

[44] R. Naaman, Y. Paltiel, and D. H. Waldeck, Nat. Rev. Chem. **3**, 250 (2019).

[45] S.-H. Yang, R. Naaman, Y. Paltiel, and S. S. P. Parkin, Nat. Rev. Phys. **3**, 328 (2021).

[46] G. L. J. A. Rikken, J. Fölling, and P. Wyder, Phys. Rev. Lett. **87**, 236602 (2001).

[47] L. Wan, Y. Liu, M. J. Fuchter, and B. Yan, Nat. Photon. **17**, 193 (2023).